Nanoscale Advances

ROYAL SOCIETY OF CHEMISTRY

PAPER

Cite this: *Nanoscale Adv.*, 2024, **6**, 1106

The chimera of 2D- and 1D-graphene magnetization by hydrogenation or fluorination: critically revisiting old schemes and proposing new ones by *ab initio* methods†

Andrea Albino, [a] Francesco Buonocore, [b] Massimo Celino[b] and Federico Totti *[a]

Graphene is an ideal candidate material for spintronics due to its layered structure and peculiar electronic structure. However, in its pristine state, the production of magnetic moments is not trivial. A very appealing approach is the chemical modification of pristine graphene. The main obstacle is the control of the geometrical features and the selectivity of functional groups. The lack of a periodic functionalization pattern of the graphene sheet prevents, therefore, the achievement of long-range magnetic order, thus limiting its use in spintronic devices. In such regards, the stability and the magnitude of the instilled magnetic moment depending on the size and shape of *in silico* designed graphane islands and ribbons embedded in graphene matrix will be computed and analysed. Our findings thus suggest that a novel and magneto-active graphene derivative nanostructure could become achievable more easily than extended graphone or nanoribbons, with a strong potential for future spintronics applications with a variable spin-current density.

Received 17th November 2023
Accepted 6th January 2024

DOI: 10.1039/d3na01008b

rsc.li/nanoscale-advances

1 Introduction

Spintronics is the study of basic physical principles underlying the generation of spin-polarized currents in semiconductors and metals.[1–4] The goal of spintronics is to understand the interaction between the particle's spin and its solid-state environments and to combine different materials to make composite devices. The prototypical kind of device is the spin valve, the term coined in 1991 by Dieny.[5]

Graphene, hereafter called G-ene for brevity, is an ideal candidate material for spintronics[6,7] due to its layered structure and peculiar weak spin–orbit coupling that facilitates spin transport and modulation of electrical properties.[8–13] G-ene is a two-dimensional (2D) allotrope of carbon isolated for the first time in 2004 by mechanical exfoliation of pyrolytic graphite.[14] Chemical vapor deposition (CVD) technique is today the most widely used because it allows to achieve large scale production.[15]

Using G-ene in possible applications, such as photodetectors, sensors, organic light-emitting diodes, organic thin film transistors, supercapacitor, and catalytic applications, photovoltaics, or spintronics, it is essential to finely modulate its electronic and magnetic properties.

It presents unusual mesoscopic effects.[16] These effects originate from the boundary conditions required for the wave functions, and depend also on the type of edges exhibited at the termination of a mesoscopic sample. The most studied edges, *zigzag* (ZZ) and *armchair* (AC),[17] have drastically different electronic and magnetic properties.[18] ZZ edges can sustain edge (surface) states and resonances that are not present in the AC case.

G-ene application in electronics suffers from a major drawback: graphene is, in its pristine state, a zero-band-gap semiconductor.[19,20] Furthermore, in the absence of d or f electrons, the production of magnetic moments is not trivial. Several ways have been explored to tune electronic structure of G-ene. It was found experimentally that a band gap can be opened by confinement effects of electrons in graphene nanoribbons,[21] or by applying a potential difference over a graphene bilayer.[22] A different approach, opening a challenging playground for chemists,[23–25] is chemical modification of pristine G-ene. The main obstacle is the control of the geometrical features and of the selectivity of functional groups.[26] The lack of periodic functionalization patterns prevents the achievement of long range ferromagnetic order, thus limiting the potentialities in applications.[27]

Hydrogenation of G-ene is an attractive solution and it is foreseen to both open a band gap and to produce a magnetic

[a]*Dipartimento di Chimica "Ugo Schiff" & INSTM RU, Università degli Studi di Firenze, Via della Lastruccia 3, Sesto Fiorentino (FI) 50019, Italy. E-mail: federico.totti@unifi.it*
[b]*Agenzia nazionale per le nuove tecnologie, l'energia e lo sviluppo economico sostenibile (ENEA), Casaccia Research Centre, Roma 00123, Italy*

† Electronic supplementary information (ESI) available. See DOI: https://doi.org/10.1039/d3na01008b

behavior.[28–32] Magnetic properties are highly dependent on the hydrogenation degree, while hydrogenation is a reversible process. In this light, hydrogenated G-ene could undoubtedly become a prominent two-dimensional nanomaterial with finely controlled properties[33] The 100% hydrogenated derivative $(C_1H_1)_n$, called graphane (G-ane), was experimentally ascertained[29,34–39] and theoretically predicted to open a band gap.[40–42] Various isomers have been reported for graphane structures, such as *boat* and *chair*,[32,43,44] with the latter as the most energetically favorable one. 1 : 1 stoichiometry can be difficult to achieve at the experimental level while partially hydrogenated scenarios can be much easier to obtain. Partial hydrogenation occurred as a misstep of full-hydrogenation process,[44] or obtained by electron-beam lithography techniques.[37] 50% hydrogenated G-ene (empirical formula, C_2H), discussed hereafter, is called graphone (G-one) (Fig. 1d and e). It shows several theoretical[45] and experimental evidences that, along with the opening of a band gap as in G-ane, a magnetic moment can be induced for partial hydrogenation. Implantation of magnetic moment by hydrogenation was achieved is several ways, by adsorption of G-ene on a substrate,[29,38,46,47] patterned hydrogenation by e-beam lithography,[48] CVD,[49] creation of H-vacancies in G-ane flakes,[50] stoichiometric fluorination,[51] substitution of fluorine atoms with different functional groups,[52] adatoms implantation.[53] Following the intensely debated topic of ferromagnetism in G-ene derivatives, magnetic ordering was detected in some of the aforementioned studies,[46,48] others showing only paramagnetic behavior.[51] The amount of introduced magnetic moment and the ordering of magnetic moments had scarce and controversial experimental evidences.[29,38,50,51] The defect-induced magnetism experimentally prompted and measured on hydrogenated G-ene derivatives[29,38] has reached only fractions of μ_B per carbon atom. It is worth mentioning that in literature it is not always clearly stated whether such values refer to the unit cell or to a single carbon atom, for instance.

Among G-one isomers, only the chair one (Fig. 1d) is found to be ferromagnetic[54] with *ca.* 1 μ_B per sp^2 C atom. The hypothetically possible magnetism of one moment unit per carbon atom, as calculated for the chair-type G-one isomer, has never been close to be achieved experimentally. The stabilization of the chair-type G-one isomer is hard to achieve due to the simultaneous need of: (i) selectivity for the 1,3,5 G-ene ring positions for hydrogenation; (ii) inhibition of migration to vicinal substitutions: (iii) inhomogeneity in the hydrogenation process and the limited coverage percentage.[47,55,56] The boat isomer (Fig. 1e), showing diamagnetic behaviour, lies several atomic units lower in energy. The stabilization of the chair *vs.* boat configuration was studied at the experimental[57] and theoretical level[58] also in the case of fluorination.

The theoretical results were replicated in this work (see ESI† for more details) and were used to benchmark the proposed computational protocol. G-ene derivatives computational studies available in literature are usually restricted to one single structure of the G-one conformational space, or G-ane's,[59,60] separately. The lack of a transversal analysis between G-one and G-ane structures, both as infinite periodic systems or as a local environment at interfaces, motivates us to enlarge the studies of the energy stability and magnetic analysis to a wider range of G-ene derivatives. Non-periodic structures were evaluated to tune the material towards maximization of spin density per unit area, leading to the new design of *islands* of G-ane diluted in a G-ene matrix.

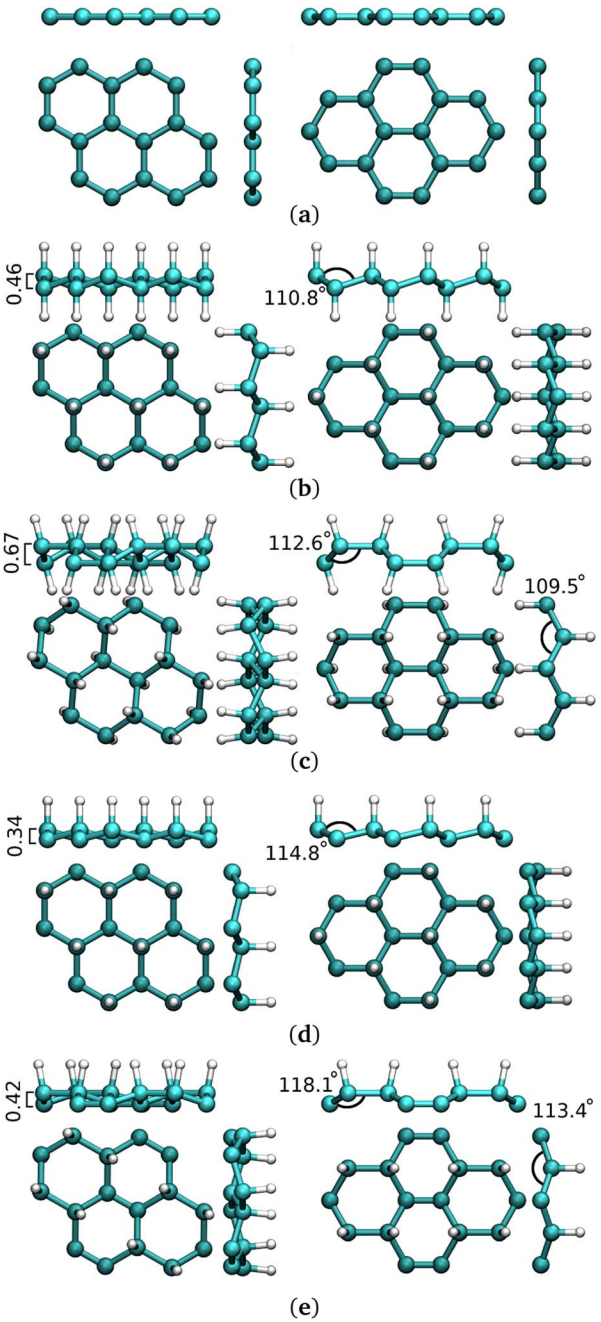

Fig. 1 Side and top views of G-ene, G-ane and G-one structures in the isolated phase. (a) Pristine G-ene. (b) Chair G-ane. (c) Boat G-ane. (d) Chair G-one. (e) Boat G-one.

2 Methods

Modeling large systems in a more realistic environment in an *ab initio* computational framework has become possible only in

the past few years thanks to overall progress of both computational resources and theoretical approaches, enabling extensive work on more and more complex systems comprising hundreds of atoms in one unit cell.[61] The modeling of surfaces through slabs within PBC showed to be mandatory to have a reliable picture of the substrate@adsorbate scenarios.[62] The packages of software CP2K were used for the periodic DFT calculations.[63] Calculation of energy and forces were performed by direct diagonalization using the Quickstep module.[64,65] Core electrons of Au, C and H elements are represented by GTH pseudopotentials.[66–68] Valence electrons for the same elements are described with pseudo-wavefunctions expanded in Gaussian-type orbitals and the density is represented in a plane wave auxiliary basis set (GPW) as implemented for the DZVP-MOLOPT-SR-GTH bases set in CP2K, SR stands here for short range and these sets were chosen to achieve a more efficient calculations of very large systems. A comparison of this basis set and the heavier version DZVP-MOLOPT-GTH is shown in Table S5 in ESI† and it highlights how the choice does not affect the results on structural, electronic and magnetic properties. The revised Perdew–Burke–Ernzerhof (revPBE) functional[69,70] was chosen for the calculation. The rVV10 non-local dispersion corrections[71] were also included. The conjugate gradient[72] (CG) minimizing procedure was employed to carry out the structure optimization. The convergence of the plane waves basis cut-off was reached for 500 Ry with a convergence threshold of 1×10^{-7} a.u. for the SCF energy and 4.5×10^{-4} a.u. per Å for the forces. The plane-waves cut-off was chosen for these systems to gain a level of precision mandatory for the study of magnetic properties and it is in the upper bound of the range used for other complex molecular magnetic systems.[73–76]

2.1 Supercell choice

Only Γ-point calculations were carried out.[77,78] The correct accounting of the symmetry and inclusion of enough k-points were assured choosing 256 G-ene unit cells to build up the supercell. A comparison of the computed electronic structure with the ones reported in literature[79] is also showed. The supercell was selected arranging three $n \times n$ arrays of G-ene non-primitive hexagonal unit cells, each containing two carbon atoms, with $n = 12, 14, 16$. The correct electronic density of states was achieved for $n = 16$ (see Fig. S1 in ESI†).

The 16×16 array of unit cells was also found to have the best matching between the Au(111) and G-ene supercells dimensions (*vide infra*). The Au(111) slab contains four layers of 192 atoms each, for a total of 768 gold atoms. A close match between substrate and adsorbate is mandatory to avoid biased interaction and consequently significant artificial stretching or compression of the two lattices. The periodicity of the substrate@adsorbate system is equal to the Au(111) surface and almost perfectly double the size of the pristine G-ene. For this reason, when designing the atom slab, an even number of G-ene rings in a row is necessary to fulfill the periodic boundary conditions (Fig. 2). The structural and cell parameters are reported in Table S1 in ESI.† A further important issue is the interactions between replica along the z axis: the finite vacuum layer thickness was here set to 70 Å to minimize this spurious contribution to the total energy.

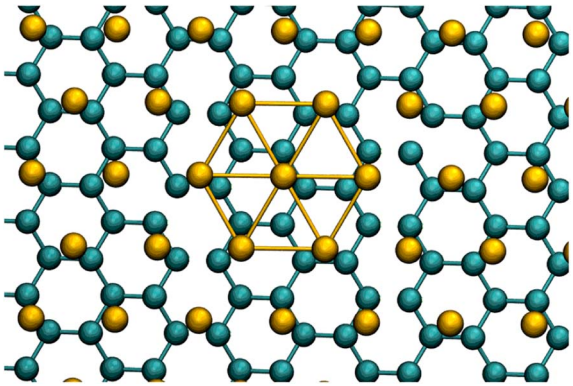

Fig. 2 G-ene@Au(111) superlattice, the lattice parameter of Au is twice the size of the G-ene structure. See DOS and structure in Fig. S8 in ESI.†

The number of atoms in the partially hydrogenated systems is the same for several structures presented in this work, allowing a stability analysis through a direct comparison of G-one and G-ane/G-ene energies. The ribbons and islands structures have an even number of H atoms; an odd number would imply the existence of an unpaired electron in the carbon backbone, that is a metastable state where the reaction with further hydrogen is very likely.[80]

All the G-ene, G-ane, and G-one supercells were also relaxed to check the error introduced by constraining their cells to the optimized Au(111) cell parameters for the subsequent simulations.

Computed lattice parameters a and b are 2.470/2.470 Å for G-ene *vs.* an experimental value of 2.46 Å;[20] 2.537/2.537 Å for chair G-one; 2.542/2.542 Å for chair G-ane; 2.568/2.589 Å for boat G-one, 2.585/2.496 Å for boat G-ane. Therefore, the above-mentioned constraining introduced an error of ~1% for chair structures and ~4% for boat structures. Being the former the only structures of interest of this study, 1% of error can be considered negligible.

2.2 Broken-symmetry state calculations for exchange coupling estimation

In the broken-symmetry, BS, formalism,[81] which is commonly utilized for quantitative estimates of exchange-coupling constants in polynuclear transition metal complexes, a one-to-one correspondence is established between the energy of a Slater determinant built up with orbitals localized on different centers and bearing electrons with opposite spin computed and the energy of a microstate with $m_S = 0$ computed using the effective Heisenberg–Dirac–Vleck spin Hamiltonian.

$$\mathscr{H}_{\mathrm{HDvV}} = J\mathbf{S}_1 \cdot \mathbf{S}_2 \quad (1)$$

where $\mathbf{S}_1$ and $\mathbf{S}_2$ are the spin values on center 1 and 2 and J is related to the multiplet energy splitting according to

$$J = \frac{E(S) - E(S-1)}{S} \quad (2)$$

In eqn (2), $E(S)$ represents the energy of a state with total spin S. J is the magnetic exchange-coupling constant, and eqn (1) is often used to reproduce experimental data. In the case of positive J, the antiferromagnetic (AF) state is the ground state; in the case of negative J, the ferromagnetic (FM) state is the fundamental one. The energy of the BS state for a binuclear system with spin $S_1 = S_2$ is a weighted average of the energies of pure-spin multiplets, and J may be calculated using the equation:

$$J = \frac{E(S_1 + S_2) - E(\mathrm{BS})}{2S_1S_2} \quad (3)$$

where E(BS) is the energy of the broken-symmetry determinant.[82,83] The term BS state means that a localized solution of the spin states is usually obtained by using an electronic symmetry lower than the actual geometric symmetry. In the present work, the G-one system contains 256 unsaturated radical carbon atoms and hence the high spin (HS) solution with total energy $E(S_{\max})$ was calculated from a ferromagnetically coupled system with $S_{\max} = 128$ and multiplicity $(2S + 1) = 257$, while the BS solution, with total energy E(BS), was calculated from the singlet state with $m_S = 0$ by imposing alternate spin-up and spin-down on the single sp^2 carbon centers. The generalization for arbitrarily large clusters is given by the formula:[84]

$$\Delta E(S_{\max} - S) = \sum_{i<j} J_{ij}\left(2|s_i s_j| + s_j\right)\lambda_{ij} \quad (s_i \geq s_j) \quad (4)$$

where $\lambda_{ij} = 0$ if s_i and s_j have the same sign in $|s\rangle$ and 1 otherwise. The J_{ij} matrix has, in G-one system, equal values for all the possible pairs of spins, and hence it can be taken out the summation as a scalar constant. Due to the high symmetry of this system, the calculation of only two determinants' energies is required. The left hand side of eqn (4) is the energy differences between the HS and the BS states, with the appropriate values of s and λ it yields all the equations needed to compute the J values.

2.3 Benchmark systems

The reliability and generalizability of a proposed computational protocol is based on the accurate reproduction of the available observables. In consideration of the fact that most of the systems considered in this work do not have or have a limited number of experimental data to be compared to, it is of basic importance to test our computational protocol on similar systems where there is an abundance of them. For such a reason, our reference calculations were performed on one layer of pristine G-ene supercell through a Γ-point approach and extended to hydrogenated and fluorinated systems already known from literature, such as G-one, G-ane, FG-one, and FG-ane. An extensive description of this benchmarking is reported in ESI† and a comparison with the existing calculations is reported in Table S1.†

3 Results and discussions

Two main approaches aimed to achieve a stabilization of the magnetic moments for homogenous and non-homogenous hydrogenation will be presented. In the first scenario, the adsorption of both types of G-one isomers on a substrate Au(111) will be tested to investigate the effects of the new substrate@surface interactions to stabilize the FM *vs.* the NM phase. In the case of non-homogenous hydrogenation, this work shows a selective patterning of hydrogenation positions to form localized islands characterized by a local G-ane structure. In this regard, a wide variety of different new hydrogenation patterns will be studied and compared to some already presented in the literature. All these systems will be studied within the same computational framework, allowing a detailed and reliable comparison of structural, energetic, and magnetic properties.

3.1 Adsorption on Au(111)

Several studies were focused on the adsorption of hydrogenated G-ene derivatives on metallic surfaces.[46,85,86] All of them make use of materials with lattice parameters not matching the G-ene one. This is not the case when using the Au(111) (or Cu(111)) surface, where an almost perfect matching with the G-ene and its derivatives can be observed.[46]

In the chair-type G-one, the hydrogenated carbon atoms positions 1,3,5 in Fig. S4 in ESI† belong to one carbon honeycomb structure sublattice while the unsaturated carbon atoms positions 2,4,6 in Fig. S4 in ESI† belong to the other one. This fact results in all the hydrogen atoms being on the same side of the G-one layer, as already stated above. The Au(111) surface could, in principle, stabilize the ferromagnetic chair-type G-one *via* the formation of extended σ/π interactions with the gold atoms positioned at a reciprocal distance commensurate to the carbon atoms one.

Both the chair- and boat-type G-one isomers deposition was simulated to quantify the energy stabilization granted by substrate–adsorbate interactions. The symmetry of the isolated G-one is lowered during adsorption on the gold surface for both isomers. In the case of the chair G-one, the unit cell is now composed by 8 atoms and the lattice parameters (2.497 Å in G-ene) become a distribution of values in the range 2.462–2.545 Å. Shorter bond lengths correspond to C_{sp^2} atoms. The single C–C bond distances stretch (1.486–1.517 Å) resulting in increased distribution of carbon atoms positions along the z axis, Δz, in the range 0.163–0.466 Å. It is worth noting that such a variation was not observed for pristine G-ene passing from the isolated to the adsorbed scenario, where the C–C bonds maintain the same lengths of 1.442 Å and Δz of 0.000 Å. The C–H bond is shrunk down to 1.120 Å (see Table S1 in ESI† for a comparison with isolated phases). The C–Au distance is in the range 2.211–2.671 Å, compared to 3.487 Å obtained for pristine G-ene adsorbed on Au(111). Shorter C–Au distances correspond to C_{sp^2} atoms. The chair-type isomer, adsorbed with the hydrogen atoms pointing away from the surface, strongly interacts with the surface retaining only 1/4 of the original magnetic moments present in

the isolated phase. The 3/4 of total sp^2 carbon atoms (192 out of 256) are in a *quasi-atop* position to the first layer of gold atoms (yellow Au atoms in Fig. 3a and b). They establish a covalent bonding interaction with Au atoms, witnessed by a significant quenching of the magnetic moment. A different situation is expected for those sp^2 carbon atoms being *atop* to gold atoms in the second layer (orange Au atoms in Fig. 3a–c). Here the C–Au bonding interactions are reduced and, therefore the quenching of the unpaired electron (carbon atoms drawn in red) is not complete. The 192 *quasi-atop* C atoms retain indeed a ~0.15–20 μ_B magnetic moment per atom, while the remaining 64 C atoms retain 0.54 μ_B per atom, that is roughly one half of the isolated system value. Even if a partial quenching of the magnetic moment was observed upon adsorption, a considerable fraction of magnetic moment is still retained.

The magnetic exchange constant *via* the broken symmetry approach was calculated, obtaining a reduction from 50 cm^{-1} to 3 cm^{-1}. Such a reduction can be explained by: (i) the distance

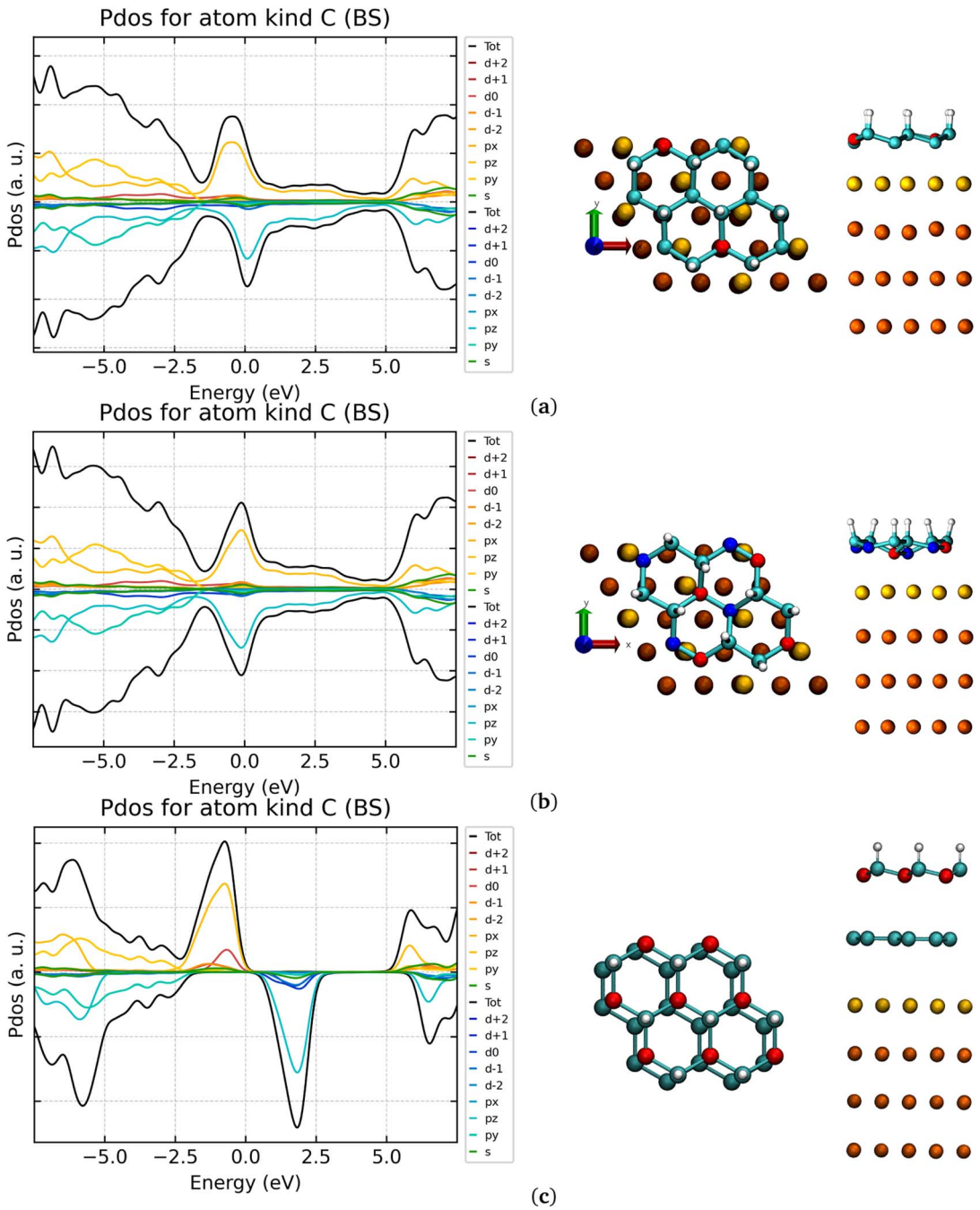

Fig. 3 (a) Chair isomer of G-one adsorbed on Au(111), DOS and sketch of the system. (b) Boat isomer of G-one adsorbed on Au(111), DOS and sketch of the system. (c) Chair isomer of G-one adsorbed on G-ene@Au(111), DOS and sketch of the system. Red/blue PDOS correspond to up/down spin.

intercurring between sp^2 carbon atoms retaining magnetic moment doubled with respect to the isolated scenario, being the spin-polarized C atoms now four bonds apart from each other; (ii) the interaction between sp^2 carbon atoms with the valence density of states of the gold surface that leads to the formation of covalent bonds. However, the retained FM behavior witnesses a certain degree of wavefunction localization, specifically in those positions where C atoms are not on a *quasi-atop* configuration to Au atoms. The Au–C_{sp^2} interaction becomes evident from the analysis of the DOS of the carbon atoms (see Fig. 3). A clear spin polarization is still evident but the band gap between the two C_{sp^2} spin components computed for the isolated scenario is filled by the new Au–C_{sp^2} covalent interactions.

For the boat-type G-one isomer, a stronger decrease of symmetry was found in comparison to chair one. The unit cell is composed of 16 atoms and the 1,3 vicinal C–C length, *i.e.* the cell parameter of G-ene, is in the range of 2.462–2.545 Å. The C–C bonds and the Δz values span wider lengths distributions compared to the chair-type G-one, 1.380–1.564 Å and 0.331–0.676 Å, respectively. The C–H bond shrunk down to 1.120 Å. The C–Au distance is in the range 2.214–2.890 Å, compared to 3.487 Å obtained for the pristine G-ene adsorbed on Au(111), the shorter distances are the C_{sp^2}–Au while the longer ones correspond to C_{sp^3}–Au distances.

The outcomes of these calculations indicate that the magnetic moment (even if partially quenched) can be maintained also in the adsorbed scenario but, unfortunately, the energy stabilization of ~3 a.u. for chair-type G-one is still not enough to make it more stable than the boat-type isomer being still ~5 a.u. more stable (see Table S1 in ESI†). The adsorbed scenario with the hydrogen atoms pointing toward the surface was not considered in virtue of the fact that the hydrogenation process can happen only on the exposed G-ene face being the other inhibited by the strong interaction with the gold surface. Only in the presence of defects, intercalation of the hydrogen atoms could take place but this will be a subject of future work.

Considering that the substitution of the hydrogen with fluorine reduced the $\Delta E_{chair-boat}$ by ~2 a.u. (Table 1), the next step of the investigation led us to the adsorption of the FG-one on the same substrate to verify if concurrent stabilization energy effects could take place. The polarization of the C–F bond has a detrimental effect on the carbon magnetic moment leading to a stronger interaction with the substrate (Au–C = 2.172–2.621 Å). A non-magnetic phase was found for both FG-one isomers, although it was expected only for the boat phase from the calculations already made on the isolated systems.

Table 1 Comparison of DFT calculated energies of G-one boat and chair isomers adsorbed on Au(111). Magnetism is the magnetic ordering of the state where the calculation converged

System	Magnetism	Energy (a.u.)
G-one chair@Au	FM	−28577.889420
G-one chair@Au	AF	−28577.887105
G-one boat@Au	NM	−28582.711844

As a further step attempting stabilization of the magnetic moment in hydrogenated and fluorinated G-ene derivatives by surface interactions, a new pristine G-ene layer was intercalated as buffer layer between Au(111) and G-one. Usually, the stacking of two G-ene layers show two kinds of symmetries called AA or AB.[87] Neither of them is obtained for the G-ene@G-one system; a configuration in between the two was nonetheless found (Fig. 3c). The structure of Au(111)@G-ene@G-one preserves the C–C bond lengths (1.483 Å) and lattice parameters (2.498 Å) of the isolated phase. The G-ene/G-one distances are in the range 3.261–3.609 Å, being the shorter distance between the G-ene_{sp^2}/G-one_{sp^2} carbon atoms and the longer the G-ene_{sp^2}/G-one_{sp^3} one. The G-ene/Au distance in Au(111)@G-ene@G-one is the same of the Au(111)@G-ene, say, 3.500 Å. Indeed, as for the structural parameters, the electronic DOS of G-one C atoms recovers the original shape observed in the isolated system (Fig. 3). An intercalated buffer layer is hence decoupling the two systems, and can be exploited to restore their original properties, thanks to the strong π-network that insulates from covalent interactions with the surface.

However, the stabilization mechanisms leaning on introduction of the Au substrate showed not to be enough to make stable FM or AF phases of G-one and FG-one.

3.2 Islands

An alternative route to instill significant spin moment in G-ene is to introduce interfaces already observed in 1D structures (*i.e.*, nanoribbons) lowering the dimensionality to 0D. In other words, systems where the G-ene is embedded in G-ane matrix. Such a scenario can be obtained saturating with hydrogen atoms specific carbon atoms rows in G-ene, or, alternatively, creating vacancies in a stoichiometric G-ane structure.[88] Moreover, contrarily to the extended systems, as G-one, where the activation barrier for H migration is very low[89] the direct and inverse H migration are limited once G-ane islands are formed.[90]

At the G-ene/G-ane interfaces, a spin polarization mechanism can be induced on the ZZ edge states,[91] and contrarily to G-ene nanoribbons, a stable injection of the magnetic moment is possible. The stability of such interfaces has been recently ascertained.[92] Furthermore, during the hydrogenation process there is a significant probability for the formation of different domains of sp^3 carbon atoms showing H frustration.[93] In other words, the ideal sequence of alternating H atoms above and below the G-ene plane is broken (frustrated) across multiple sp^3 domains, leading to the impossibility to achieve complete hydrogenation, and consequently, to the presence of some sp^2 carbon atoms domain interposed to different sp^3 domains. This aspect makes the strategy of building small domains of fully hydrogenated G-ene appealing because of the presence of fewer constrains in the design of multiple adjacent domains and its potentiality as feasible way to implant magnetic moments in G-ene with the perspective of a controlled patterning and scaling-up on the G-ene backbone.[48,94] The electronic properties of such systems are similar to a free standing G-ene nanoribbon[95] being the spin-polarized states localized in the sp^2 G-ene domain. The

spin-polarization is extended up to the 1,3 vicinal spin-polarized sp^2 carbon atoms.[95,96]

The rows of C_{sp^2} atoms in the G-ene domain in the vicinity of the interface are composed of ferromagnetically coupled spins; when the geometric pattern of the hydrogenation allows for the formation of non-communicating rows (like two opposite sides of a ribbon or the borders of an island whose continuity is disrupted by the lack of vicinal 1,3 sp^2 C atoms), each row tends to be antiferromagnetically coupled to the others. Therefore, the ground state of such systems is overall antiferromagnetic. The study of these systems shows that the spin population on each edge reaches a plateau value of 0.25 μ_B per unit cell when they are at least 12 C_{sp^2} rows far apart. Such a result indicates that a significant magnetic moment can be instilled but, at the same time, that a high density of hydrogenated portions, *i.e.*, one or two C_{sp^2} rows apart, cannot be achieved due to the competing quenching of the momentum.

To overcome this limitation and to test an alternative way to maximize the magnitude of magnetic moment per unit cell, we investigated the possibility of spin moment implantation when the 1D dimensionality of the ribbon structure is further lowered to 0D islands, allowing a richer design of the interfaces. A rationalization of the implanted magnetic moment will be presented as a function of several order parameters: the island dimension, shape, structure, and termination.

The implantation of magnetic moments in hydrogenated G-ene was pursued juxtaposing it to the chair isomer of G-ane, that is the most stable structure that is ought to form in large abundance and to be stable in thermodynamically driven reactions, for instance undergoing an annealing step after the hydrogenation process.[40] Among stoichiometric G-ane compounds, $(C_1H_1)_n$, the chair isomer is the most stable structure (Fig. 1a),[41,97] as confirmed in literature where several other structures were considered.[60] Therefore, it is likely to expect that, during the hydrogenation process, islands of this isomer can form in larger amount, or it can gradually grow at the expenses of other structures[40] during annealing.

The structures considered hereafter are not composed by homogeneous coverages, rather by islands with isolated spots with different hydrogenation content, ranging from 2 to 50%. The rationalization of different magnetic properties was possible from the analysis of prototypical systems.

3.2.1 The stability as a function of the sp^2/sp^3 interface. The interface between G-ene and G-ane shows two possible geometries, the AC, also called *boat-like* edges, and ZZ, also called *chair-like* edges[98] (see Fig. S10 in ESI†). Looking at one hexagonal ring shared between sp^2 (G-ene) and sp^3 (G-ane) portion, AC edges can be composed in one possible way, either for the boat isomer or for the chair isomer as shown in Fig. 4a and b. This interface ensures a strong bonding of adjacent 1,2 vicinal sp^2 C atoms and hence a truly diamagnetic state (NM). ZZ edges, on the other hand, may be composed in two ways, say α and β.[91] The interfaces differ for the number of hydrogenated sp^3 C atoms lying in the interfacial ring: in Fig. 4, two atoms in a and b, three atoms in c and d, five atoms in e and f. The ZZ edges are formed by C atoms belonging to the same G-ene sublattice (highlighted in red) because they are related by (1,3) meta vicinity and they are also allowed for the Lieb theorem to bear magnetic moments that order ferromagnetically.

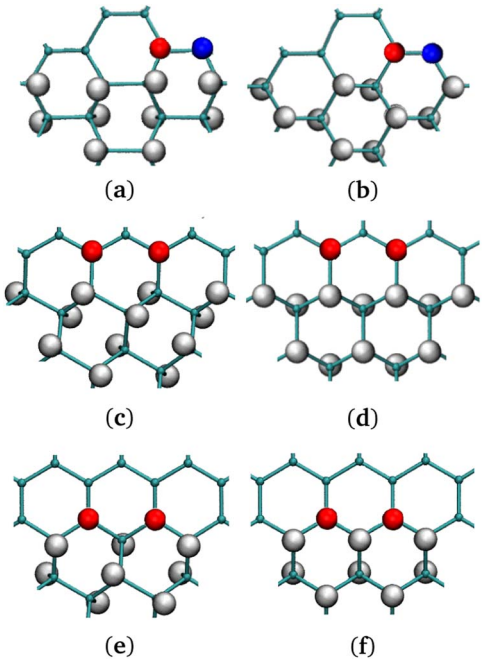

Fig. 4 (a), (c), (e) Chair G-ane isomer at the interface with G-ene. (b), (d), (f) Boat G-ane isomer at the interface with G-ene. (a), (b) AC, (c), (d) ZZ-α, (e), (f) ZZ-β terminations of G-ane domain. Two carbon atoms belonging to the nearest neighbor row are shown: the red C atoms are part of sublattice A, the blue of the sublattice B. Check Fig. S9 in ESI† for the definition of a row.

A set of island structures composed by the G-ane chair-type isomer (Fig. 1d) with AC, ZZ-α and -β edges was simulated. Being the sp^3 domain constituted by 256 H, a direct comparison of the energies with the G-one structure containing the same number of H atoms is possible, ascertaining that the islands are far more stable than boat-type G-one (Fig. 1b) by about 8 a.u. (see Table 2).

The AC and the ZZ-α edges are the ones with the lowest energies which differ by only 0.06 kcal mol^{-1} (0.026 eV) in favor of the former. Such a result is of extreme importance, since it indicates that both are equally favorable at room temperature in

Table 2 Comparison of DFT calculated energies of G-ane boat and chair isomers island embedded in G-ene with all possible termination edges: AC, ZZ-α, ZZ-β

System	Isomer	Edge	Energy (a.u.)	Ref.
G-ane/G-ene	Chair	AC	−3063.710216	Fig. 5a
G-ane/G-ene	Chair	ZZ-β	−3062.999279	Fig. 5b
G-ane/G-ene	Chair	ZZ-α	−3063.709245	Fig. 5c
G-ane/G-ene	Boat	AC	−3062.971278	Fig. 5d
G-ane/G-ene	Boat	ZZ-β	−3062.21740	Fig. 5e
G-ane/G-ene	Boat	ZZ-α	−3062.673169	Fig. 5f
G-one	Chair	—	−3046.569877	Fig. 1d
G-one	Boat	—	−3054.784962	Fig. 1e

a G-ane matrix,[59,92,95,99] contrarily to the case of freestanding nanoribbons, where it was found that the ZZ edge is metastable and a planar reconstruction occurs leading to lower energy AC edges.[98] The spin density is distributed along the ZZ-α edges and it is larger at the center of the row, decreasing towards the ends. From here on, only ZZ-α edges will be considered for the next systems under study. When dealing with 0D structures, several kinds of edges must coexist because the interface of a 0D island describes a closed path. As already mentioned, the edges reported in Fig. 4 are studied for a series of G-ane islands made of 256 H atoms and for each of them a prevalent edge type has been arranged at the interface (see Fig. 5 for complete island structure) and bound by different types of junctions.

In such a framework, it is interesting to notice that different island corners can be obtained. They are characterized by the 1,3 or the 1,4 patterning which have different effects on the propagation of the spin polarization present along the island sides. Such a behavior will be studied in detail in the next paragraph.

3.2.2 The effect of the junction between ferromagnetic rows. To rationalize the origin of the magnetic moment, several clusters of G-ene of different sizes were considered. Terminal carbon atoms were saturated by hydrogen atoms. Different G-ene/G-ane interfaces of different shapes and extensions were then created by adding H atoms (see Fig. S10a in ESI†) in the middle of the G-ene structure to obtain either completely separated or communicating sides. In the former case, the direct interaction between the interface states across the G-ane region is negligible, and symmetric localized degenerate states are expected for the two sides for the AF state. If the two interfaces are put in communication through a G-ene corner with a 1,4 patterning (Fig. S10b in ESI†), the wavefunction loses its symmetry leading to a delocalized magnetic orbitals, strongly quenching the residual magnetic moment. This is mainly due to the disruption of the 1,3 (meta) arrangement of polarized sp^2 carbon atoms at the interphase that favour an FM polarization.

Indeed, it was found that a continuity in the 1,3 patterned C atoms across a sharp corner (Fig. S10c in ESI†) led to retention of the spin polarization. To confirm this outcome, several other junctions were considered. For instance, an obtuse angle between ZZ edges (Fig. S10d in ESI†) leads again to 1,4 pattern of the C atoms at the sp^2/sp^3 interface, forbidding a FM spin polarization. This type of junction becomes a point where the FM spin rows invert their polarity. AC (Fig. 4a and b) edges may be formed by the junction of ZZ rows (Fig. S10e in ESI†). They have the same feature of triggering the spin polarity inversion, but they are less efficient than the previous ones because they lead to the quenching of spin moment across them, lowering the total density of spin population per unit area.

3.2.3 Minimum island extension to generate spin density and total spin population implanted in a row. Once the effect of quenching of the spin polarization mechanism made by 1,4 type junctions was tested, we investigated if and how such an effect could be detrimental for total magnetic moments for a single side of the junction. Therefore, a series of islands were built for this purpose. In particular, a series of nanoribbons of G-ane extending from 2 to 13 sp^3 C rings (see Fig. S11 in ESI†) are embedded in the 512 C atoms G-ene slab already used for the other prototypes. The G-ane C rings are juxtaposed to form a condensed C rings structure. The longest row that can be composed in our computational framework contains 16 G-ane C rings and it reaches the boundaries of the carbon slab giving rise to a 1D nanoribbon structure (see Fig. S12 in ESI†). Interestingly, a dependence of the average moment of sp^2 C atoms at the ZZ sp^2/sp^3 interface on the G-ane nanoribbon length (Fig. 6 and Table 3) was observed. The 16 condensed C rings systems

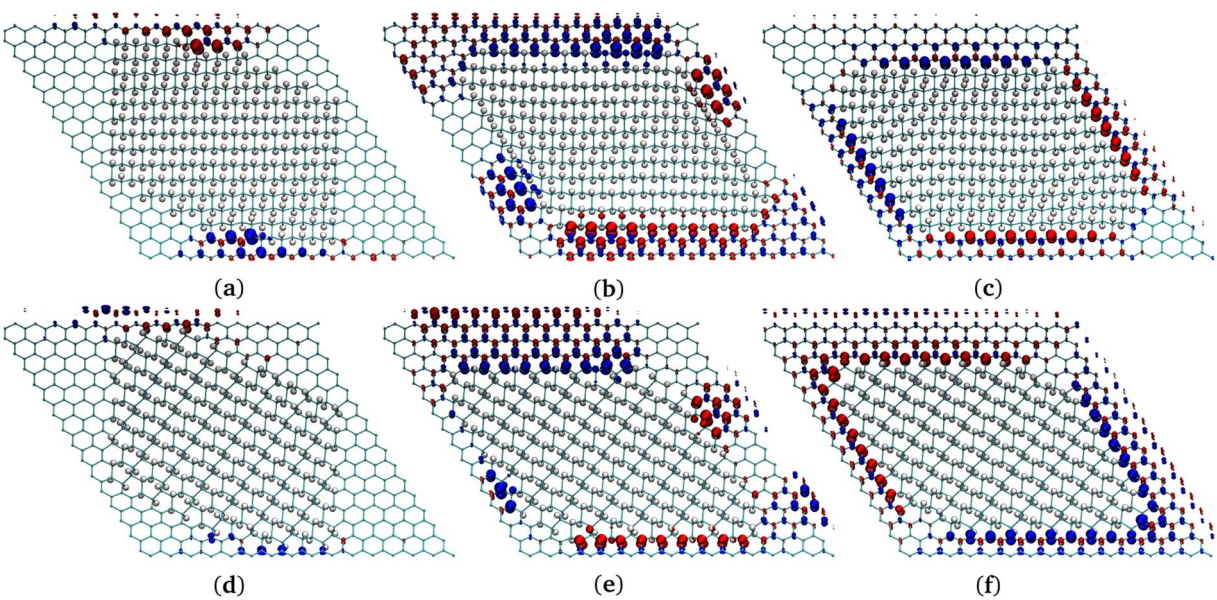

Fig. 5 AC (a and d), ZZ-α (b and c), and ZZ-β (e and f) termination of chair (a–c) and boat (d–f) G-ane in G-ene/G-ane interface. Two carbon atoms belonging to the nearest neighbor row are shown: the red C atom is part of sublattice A, the blue of the sublattice B. Red/blue is the $\pm$ spin density.

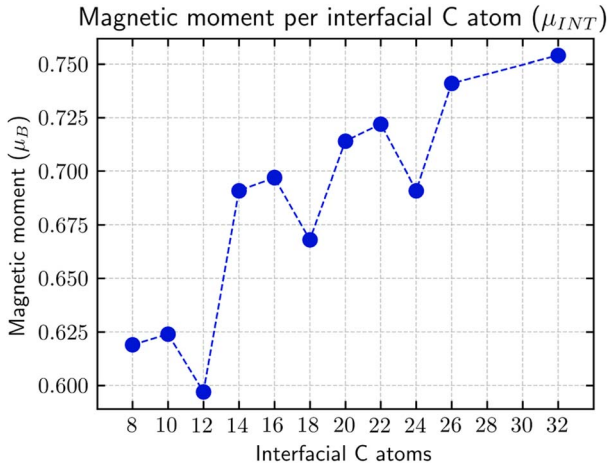

Fig. 6 α and β magnetic moment per interfacial C atom $\mu_{INT} = \frac{(|\alpha| + |\beta|)}{C_{INT}}$. The unit for magnetic moments is μ_B. Fig. S11 and S12 in ESI† show the systems analysed in this series, data are collected in Table 3.

yields the maximum value of 0.75 μ_B across the series. Such a value is in agreement with the one reported in the literature for simulated fully periodic nanoribbons[96] and those experimentally measured even if on SiC (0.1 μ_B (ref. 29) and 0.45 μ_B (ref. 38)). For very short nanoribbon lengths, *i.e.*, up to 3 C condensed rings atoms, no magnetic moment is retained. From 4 up to 13 an increase of the magnetic moment reaching $0.377(-0.377)\mu_\alpha(\mu_\beta)$ was computed. The observed trend can be explained by the existence of 1,4 AC junctions-type at the nanoribbons ends, which lead to a decrease of the magnetic moment of the carbons in their proximity up to the quenching of it exactly at the junction. In Table 3 are reported the number of C_{sp^2} atoms the lie facing directly the G-ane portion and form a chain of 1,3 vicinal atoms (C_{INT}). They belong to the same sublattice and can align their magnetic moment according to Lieb theorem. The converged calculations show that these atoms carry the majority of the magnetic moment implanted after hydrogenation. Such results unveiled that the size and, therefore, the sides of a G-ane island need to obey a compromise for the best combination between the dimension of G-ane/G-ene interface and magnetic moment per sp^2 C atom.

The only structure that did not converge was the 14 G-ane condensed rings nanoribbon, *i.e.*, the one that has only two G-ene C rings separating the G-ane nanoribbon. The 15 C rings structure was not designed because it would reach one of the boundaries of the used carbon slab and would give rise to a 29 rings structure that exceed the designed series. A spin frustration at the junctions of two nanoribbons, too close to each other, could be claimed as the cause for such discontinuity.

The origin of the plateau value reached for $n > 7$ can be explained by the formation of a valence/conduction band. The C atoms at the edge (ZZ sp^2/sp^3 interface) theoretically possess a total magnetic moment of 1 μ_B, but, due to the periodic ripples induced by the interface, a large part of the energy degeneration in the Fermi region is removed. Such an effect is of extreme importance since it limits the increase of the instilled magnetic moment proportionally to the number of the C_{sp^2} atoms.

Looking at the evolution of the DOS depending on the length of the G-ane nanoribbon, it can be observed that a Dirac cone-like structure is maintained for all the length values but with the difference that the Fermi energy is shifted from the Dirac point towards the occupied states. Such behavior is expected due to the break up of the G-ene π system because of the formation of σ C–H bonds which contribute to increasing the number of bands around Fermi and makes them asymmetrically populated with respect to it.

3.2.4 Influence of the distance between ZZ sp^2/sp^3 interfaces. Another parameter to consider when implanting magnetic moment in G-ene by selective hydrogenation is the distance between the G-ane islands. It is reported in literature that for two nanoribbons separated by a number of C_{sp^2} rows, n, (see Fig. 7), the computed magnetic moment decreases from a plateau value of 2/3 μ_B for $n = 12$ to 0 for $n = 3$.[96] The width of sp^2 portion can hence directly influence n and, consequently, the spin density at the ZZ sp^2/sp^3 interfaces. To confirm the dependence of spin density as a function of n, three supercells with single ($n = 3$), double ($n = 7$), and fourfold ($n = 15$) two-rows-wide G-ane nanoribbons were generated (Fig. 7) within the same computational framework of the system presented in this work. In the case of the computed magnetic moment per interfacial C_{sp^2} atoms ($\mu_{INT}{}^{\alpha} = |\mu_\alpha|/C_{INT}$), the results are in agreement with the literature:[96] a value of 0.378 μ_B was computed for $n = 15$, while decreasing moments of 0.328 μ_B and 0.171 μ_B were observed for $n = 7$ and $n = 3$, respectively (see Table 4). Due to the adoption of the same 512 C atoms slab, we

Table 3 Comparison of spin densities of the series of two-rows-wide islands composing an integer number of condensed hexagonal rings from 2 to 16. The 16 condensed rings system reported is a 1D nanoribbon. Structures are showed in Fig. S11 and S12 in ESI. Each slab contains a total C atom number of 512 (256 G-ene unit cells). C_{sp^2} are the C atoms in the G-ene portion of material. C_{INT} are the interfacial sp^2 C atoms facing the G-ane sp^3 portion and showing a 1,3 vicinity relationship among each other. $\mu = |\mu_\alpha| + |\mu_\beta|$. $\mu_{unit\ cell} = \frac{(|\alpha| + |\beta|)}{256}$. $\mu_{sp^2} = \frac{(|\alpha| + |\beta|)}{C_{sp^2}}$. $\mu_{INT} = \frac{(|\alpha| + |\beta|)}{C_{INT}}$. The unit for magnetic moments is μ_B. See Table S7 in ESI for μ_α and μ_β

Rings	H	C_{sp^2}	C_{INT}	μ	$\mu_{unit\ cell}$	μ_{sp^2}	μ_{INT}
2	10	502	4	0	0	0	0
3	14	498	6	0	0	0	0
4	18	494	8	4.95	0.0193	0.0100	0.619
5	22	490	10	6.24	0.0244	0.0127	0.624
6	26	486	12	7.16	0.0280	0.0147	0.597
7	30	482	14	9.67	0.0378	0.0201	0.691
8	34	478	16	11.15	0.0436	0.0233	0.697
9	38	474	18	12.03	0.0470	0.0161	0.668
10	42	470	20	14.28	0.0558	0.0304	0.714
11	46	466	22	15.88	0.0620	0.0341	0.722
12	50	462	24	16.59	0.0648	0.0359	0.691
13	54	458	26	19.26	0.0752	0.0421	0.741
14	58	454	28	—	—	—	—
16	64	448	32	24.12	0.0942	0.0538	0.754

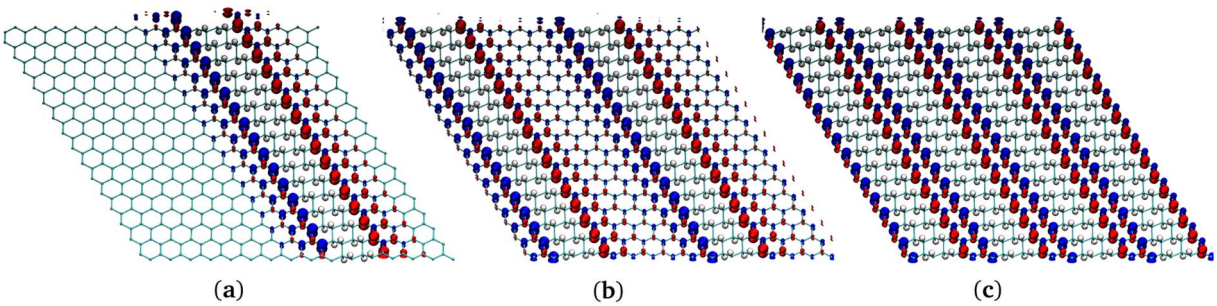

Fig. 7 Comparison of structures of several G-ane/G-ene systems with nanoribbon patterns. (a) One nanoribbon. (b) Two nanoribbons. (c) Four nanoribbons.

Table 4 Comparison of spin densities of several G-ane/G-ene systems with nanoribbon patterns. Each slab contains a total C atom number of 512 (256 G-ene unit cells). C_{sp^2} are the C atoms in the G-ene portion of material. C_{INT} are the interfacial sp^2 C atoms facing the G-ane sp^3 portion and showing a 1,3 vicinity relationship among each other. $\mu = |\mu_\alpha| + |\mu_\beta|$. $\mu_{unit\ cell} = \frac{(|\alpha| + |\beta|)}{256}$. $\mu_{sp^2} = \frac{(|\alpha| + |\beta|)}{C_{sp^2}}$. $\mu_{INT} = \frac{(|\alpha| + |\beta|)}{C_{INT}}$. The unit for magnetic moments is μ_B. See Table S8 in ESI for μ_α and μ_β

H	C_{sp^2}	C_{INT}	μ	$\mu_{unit\ cell}$	μ_{sp^2}	μ_{INT}
1 × 64	448	32	24.12	0.0942	0.0538	0.754
2 × 64	384	64	42.04	0.164	0.109	0.656
4 × 64	256	126	43.82	0.171	0.171	0.348

could directly compare the total magnetic moment per C atom as a function of n. Interestingly, despite the decrease for small n values of the magnetic moment per interfacial C atom, the total μ in the system with $n = 3$ is almost doubled compared to the system with $n = 15$ (see Table 4). The reduction of the magnetic moment per C_{sp^2} with the decrease of n can be explained by the reduction of the degenerate states at the interface. Nevertheless, at least at the theoretical level, a higher ratio of sp^3/sp^2 atoms is preferable. Such result pinpoints the optimal distance between islands in a G-ene matrix to maximize the magnetic moment per C atom, *i.e.*, per unit area of carbon backbone.

3.2.5 The pathway toward the increase of magnetic moment by G-ane islands and nanoribbons. To the best of our knowledge, a comprehensive study on the possible strategies to use to maximize the instilled magnetic moment in the G-ene by selective hydrogenation is not available in literature. For this reason, the rules we derived describing the dependence of the instilled magnetic moment, *i.e.*, on the length of the G-ane nanoribbon and on the distance and the junctions between them, need at this stage to be exploited. In this regard, several different structures were generated for a direct comparison: ribbons (Fig. 7) and islands (Fig. 8). Additionally to what is already in literature, where only ribbons were considered and only the amount of instilled magnetic moment per C atom was reported, we will compare also their relative thermodynamic stability. Therefore, for the sake of consistency, the total energy of systems with the same number of H atoms will be compared. Several systems were composed varying the number of hydrogens bonding to the pristine G-ene layer: 64H, 96H, 200H, and 256H. The subscript nr or is in the following stands for nanoribbons or islands, respectively.

The design of the islands is based on the following insights to achieve the highest instilled magnetic moment in the G-ene portion of the material:

(i) ZZ-α sp^2/sp^3 interface (Fig. 4d);

(ii) Consider as many 1,3-type junctions to connect the ZZ-α sp^2/sp^3 interfaces to make a closed-path and generate a 0D structure;

(iii) Islands with sides greater than 4 and smaller than 14 G-ane rings in consideration of the computed dependence of the magnetic moment with the length of the interface;

(iv) The minimum distance between two ZZ-α sp^2/sp^3 interfaces, n, has to be set not lower than 3.

3.2.5.1 64H and 256H. The two systems in Fig. 8a and e were chosen to establish a direct energy comparison to the G-ane nanoribbons (Fig. 7a and c) as a function of the not hydrogenated/hydrogenated (sp^2/sp^3) ratio. The 256 H systems also allow a direct energy comparison with the most stable isomer of G-one, the boat-type. In both 64H and 256H cases, the islands showed to be much more stable than the correspondent nanoribbon (688 and 78 kcal mol^{-1}, respectively) indicating that islands can effectively represent a stable alternative (see Table 5).

However, the nanoribbons have shown to be able to stabilize 0.75 μ_B per interfacial C_{INT} atom and 0.054 μ_B per C_{sp^2} atom (64H system in Table 4). Such values are higher than those achieved for the islands: a larger spin polarization of 0.79 μ_B was achived for C_{INT} but almost a half of the value, 0.034 μ_B, per C_{sp^2} atom (64H system in Table 6). When looking at the 50% hydrogenated systems, the island has a higher value of retained magnetic moment per C_{INT}, but the overall magnetic moment stabilized in the slab is higher for the ribbon (256H in Tables 4 and 6). Of course, if these data are compared with the ones that can be obtained with the homogeneous hydrogenation process of G-ene, *i.e.*, with the G-one, it comes out that only a fraction of the magnetic moment per unit cell (or per C_{sp^2}) can be obtained by the heterogeneous hydrogenation of G-ene. Despite all this, such a fraction of instilled spin, being in the range of 5–11%, can still be suitable for spintronic applications. This is an

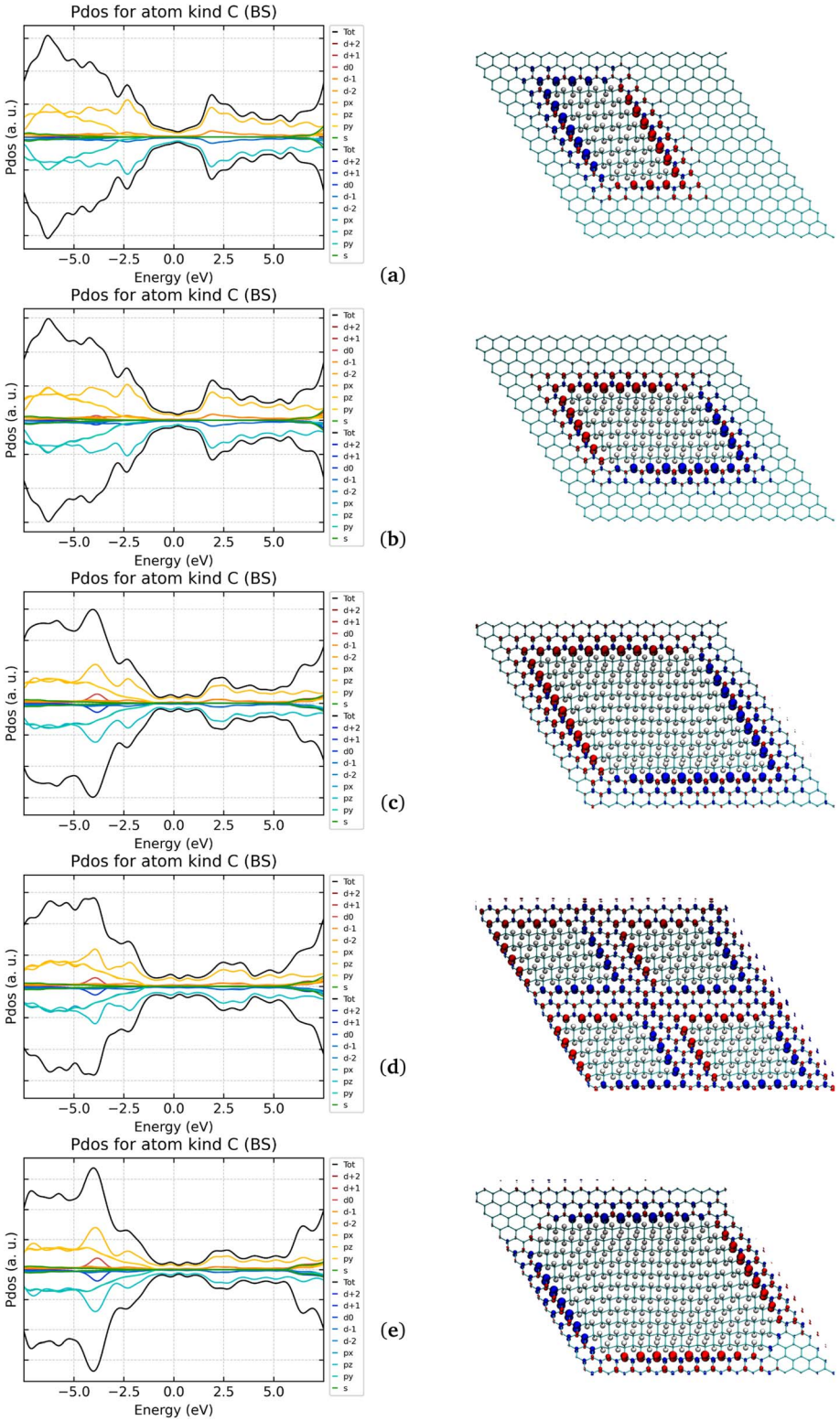

Fig. 8 Comparison of electronic DOS and structures of several G-ane/G-ene systems with island patterns. (a) 1 × 64H_{is}. (b) 1 × 96H_{is}. (c) 1 × 200H_{is}. (d) 4 × 50H_{is}. (e) 1 × 256H_{is}. Red/blue PDOS correspond to up/down spin.

appealing results because it clearly indicates that G-ane islands are by far the most thermodynamically stable systems compared to both G-one and G-ane nanoribbons. Because of the hydrogenation, a semioccupied band at the Fermi energy was observed for all the systems with a Dirac cone shifted of ∼0.2 eV at higher energy (Fig. S12 in ESI†).

Table 5 Comparison of total energy of several G-ene/G-ane systems with nanoribbon or island patterns. Each slab contains a total C atom number of 512 (256 G-ene unit cells). C_{sp^2} are the C atoms in the G-ene portion of material

H	C_{sp^2}	Nanoribbon (a.u.)	Island (a.u.)	G-one boat (a.u.)
64	448	−2950.370277	−2950.494546	—
256	56	−3062.612797	−3062.673169	−3054.784962

Table 6 Comparison of spin densities of several G-ane/G-ene systems with island patterns with FM chair isomer of G-one (last line "G"). Each slab contains a total C atom number of 512 (256 G-ene unit cells). C_{sp^2} are the C atoms in the G-ene portion of material. C_{INT} are the interfacial sp^2 C atoms facing the G-ane sp^3 portion and showing a 1,3 vicinity relationship among each other. μ_α is the alpha spin density. μ_β is the beta spin density. $\mu = |\mu_\alpha| + |\mu_\beta|$. $\mu_{\text{unit cell}} = \frac{(|\alpha| + |\beta|)}{256}$. $\mu_{sp^2} = \frac{(|\alpha| + |\beta|)}{C_{sp^2}}$. $\mu_{INT} = \frac{(|\alpha| + |\beta|)}{C_{INT}}$. The unit for magnetic moments is μ_B. See Table S9 in ESI for μ_α and μ_β

H	C_{sp^2}	C_{INT}	μ	$\mu_{\text{unit cell}}$	μ_{sp^2}	μ_{INT}
1 × 64	448	24	15.20	0.0590	0.034	0.633
1 × 96	416	28	17.82	0.0696	0.0428	0.636
1 × 200	312	40	25.00	0.0961	0.0789	0.801
4 × 50	312	80	29.75	0.116	0.0954	0.372
1 × 256	256	42	19.85	0.0775	0.0775	0.473
G-one	256	256	243.00	0.949	0.949	0.949

3.2.5.2 $64H_{is}$, $96H_{is}$, $200H_{is}$, and $256H_{is}$. The island solution can be an effective strategy, showing how the magnetic moment could vary in function of the amount of hydrogenation is the next step. In Fig. 8, the systems where two descriptors change at the same time: (i) the number of C_{INT} atoms at the sp^2/sp^3 interface; (ii) the extent of the sp^2 portion between adjacent islands.

The computed results indicate that the μ can be increased by a constant value of *ca.* 0.63 μ_B per single C_{INT} until a limiting distance among them is maintained (seven C rings in the 1 × $200H_{is}$ system). In other words the balance of the C_{INT}/C_{sp^2} ratio matters and when the distance between the C_{INT} falls below seven C rings, the μ drops from 25 μ_B (1 × $200H_{is}$) to 19.85 (1 × $256H_{is}$). It is worth mentioning that another cause of the quenching of the magnetic moment is present in the $256H_{is}$. Indeed, at the difference of all the other cases where the same junctions-type were used, the two 1,3 sharp corners had to be "smoothed" by the introduction of a small three-rings-long side connected to the adjacent ones by 1,4 junctions. The latter are known from previous paragraphs to quench the magnetic moment and, therefore, the obtained value of 0.0775 μ_B can be ascribed to that. No significant differences were observed for the DOS but the increase of the energy gap (ex G-ene Dirac cone) for the system with the highest hydrogenation coverage (0.06 and 0.11 eV for $200H_{is}$ and $256H_{is}$, respectively. See Fig. 8).

3.2.5.3 $200H_{is}$ (one island) & $200H_{is}$ (four islands). Among the single island models, the $200H_{is}$ shows the largest magnetic moment per unit cell, since the system in Fig. 8 was built to maximize the number of the C atoms at the sp^2/sp^3 interfaces at the detriment of their distances dividing the single island with four equivalent ones. The number of polarized C atoms was then doubled (from 40 to 80) and, consequently, the interfaces distances were halved (from $n = 6$ to 3). Indeed, the doubled number of C_{INT} atoms did not lead to a doubled value of μ, since μ_{INT} dropped from 0.63 to 0.37 μ_B right because of the reduced distance between the "magnetic" interfaces. However, a further increase of μ was observed (from 25.00 to 29.75 μ_B) so that a value of 0.12 μ_B per cell was reached. The use of same number of atoms in the 1 × $200H_{is}$ and 4 × $50H_{is}$ cells allowed to directly estimate their enthalpic stability: Unfortunately, the former is far more stable than the latter of 346 kcal mol^{-1}. Anyhow, the above results paved the way for the reach of best engineering between the number of C_{INT} and the distance between the magnetic interfaces they belong to.

3.2.6 Adsorption on Au(111) and Au(111)/G-ene. In order to prove the applicability of the most promising systems in potential devices, the $200H_{is}$ system, both in the single and four islands patterns, were adsorbed on different substrates: on a clean unreconstructed Au(111) surface and on a buffer layer of G-ene deposited on the same gold surface. Unlike the Au(111)@G-one, where no hydrogen atoms were present between the gold surface and the G-one carbon skeleton, the two chosen $200H_{is}$ systems present half of their H atoms pointing towards the substrate. In principle, their presence could prevent an effective overlap between the C_{sp^2} π/π^* system and the gold conduction/valence bands, a scenario that was already found for the G-one@Au(111) and that determined a relevant quenching of the magnetic moment of the adsorbate.

3.2.6.1 $200H_{is}$(1)@Au(111) (one island) & $200H_{is}$(4)@Au(111) (four islands). A relaxation of the adsorbate for better interaction with the gold surface was observed. In particular, the evident ripples in the G-ane islands got significantly reduced leading to an overall $200H_{is}$ flattened structure. Such a reorganization maximized the adsorbate/substrate interaction which is witnessed by the stretching of the C–H bonds and, to a lesser extent, a shrinking of the C–C ones (see Table S10 and Fig. S13 in ESI†).

However, as a downside of longer C–H elongations, a quenching of the magnetic moment at the expenses of the respective carbon atoms was observed. This can be explained by the partial homolytic cleavage of the C–H bonds with the concurrent formation of the Au–H one, as a consequence of the strong affinity of the two elements. In the $200H_{is}$(1)@Au(111) scenario the complete quenching interested not only the C atoms at both 1,3 and 1,4 junctions, where the C–H distances are larger, but also two/three more C atoms for single interfaces (island sides): the result is that four/five C atoms have a quenched magnetic moment *versus* a total of ten atoms that are polarized in the isolated scenario (see Fig. 8c and S14 in ESI†). Eventually, the magnetic moment retained is 2/3 of the latter (see Table 7) and it has to be compared to the 1/4 of the amount retained for G-one@Au(111).

Such results indicate that a surface with less affinity towards the hydrogens would be better suited to maintain the magnetic

Table 7 Comparison of spin density of 200H islands G-ane/G-ene system, when adsorbed directly on Au(111) or on the Au(111)@G-ene system (buffer). Each slab contains a total C atom number of 512 (256 G-ene unit cells). C_{sp^2} are the C atoms in the G-ene portion of material. C_{INT} are the interfacial sp^2 C atoms facing the G-ane sp^3 portion and showing a 1,3 vicinity relationship among each other. μ_α is the alpha spin density. $\mu = |\mu_\alpha| + |\mu_\beta|$. $\mu_{\text{unit cell}} = \frac{(|\alpha| + |\beta|)}{256}$. $\mu_{sp^2} = \frac{(|\alpha| + |\beta|)}{C_{sp^2}}$. $\mu_{INT} = \frac{(|\alpha| + |\beta|)}{C_{INT}}$. The unit for magnetic moments is μ_B. See Table S9 in ESI for μ_α and μ_β

Buffer	H	C_{sp^2}	C_{INT}	μ	$\mu_{\text{unit cell}}$	μ_{sp^2}	μ_{INT}
No	200	312	40	9.95	0.0389	0.0319	0.249
Yes	200	312	40	14.08	0.0550	0.045	0.352

moment in selectively hydrogenated G-ene derivatives and that no spin polarization could be likely obtained when the total number of C atoms for a single sp^2/sp^3 interface is smaller or equal to five. In this regard, the other promising system, $200H_{is}(4)$@Au(111), which is formed by four islands with five C_{sp^2} atoms per side and the same number of 1,2 and 1,4 junctions of the $200H_{is}(1)$, showed revealing results. As expected, a total quenching of the magnetic moment was then observed.

Such results gave a mixed picture. They confirmed that it was possible to retain a certain amount of magnetic moment for heterogeneous hydrogenated G-ene derivatives on a metal surface but at the same time suggested that this is possible if the number of C atoms at the sp^2/sp^3 interfaces are larger than a critical value. The latter consideration derives from the asymmetric Au–H interactions due to the G-ane island ripples.

3.2.6.2 $200H_{is}$@G-ene, $200H_{is}$@Au(111)/G-ene. Taking advantage of the above results, a buffer layer of G-ene was introduced between the $200H_{is}$ systems and the Au(111) surface. As in G-one@Au(111)/G-ene where the magnetic moment was almost totally retained, the aim was to decouple the surface from the adsorbate to avoid strong interactions which could lead to a quenching of the magnetic moment. At the structural level, the ripples in the C atoms skeleton are still maintained even if to a smaller extent than the isolated scenario. The C–H bond variations, although present, are hence less pronounced than in the $200H_{is}(1)$@Au(111). Consequently, some quenching of the magnetic moment was found even in this case. However, even if more limited than in the $200H_{is}(1)$@Au(111) scenario, the original spin polarization of the C atoms at the sp^2/sp^3 interface was significantly retained: 0.35 μ_B for Au(111)/G-ene *vs.* 0.25 μ_B per interfacial C atom when the substrate is Au(111). Such a result is very promising since it suggests that the implantation of technologically relevant spin polarization can be achieved in such a kind of systems.

4 Conclusions

The quest for magnetic materials for spintronics has been pushed forward, seeking at implantation of stable magnetic moments on covalently hydrogenated graphene. The formation of covalent bonds between carbon atoms and other species (*e.g.*, hydrogen and fluorine) strongly affect the electronic properties and local structure of the material (*i.e.* changing from sp^2 to sp^3 carbon hybridization). This process, however, does not explicitly instill unpaired electrons in the system, and, therefore, the counter-intuitive resulting establishment of localized spin moments in the new G-ene derivatives has been shown to be a valuable way to forward. We investigated several avenues to obtain, at the *in silico* level, a stable magnetic phase for hydrogenated G-ene. To overcome the magnetic instability which favors the diamagnetic states for hydrogenated G-ene derivatives, two main approaches have been tested: (i) the adsorption of hydrogenated G-ene layer on a substrate (gold and pristine G-ene, or the latter used as buffer layer on the former) to check whether the formation of new surface interactions could stabilize the FM phase; (ii) the partial patterned hydrogenation of carbon backbone by means of densely hydrogenated C atoms islands, forming locally a G-ane structure, surrounded by G-ene matrix. The first strategy was found to generate a strong surface–adsorbate interaction that basically reduces the magnetic moment of G-one, while the second one consisted in the formation of 0D hydrogenated structures. The latter disclosed new possibilities to obtain stable systems with the formation of a sizable magnetic moment at the sp^2/sp^3 interface portions of the material through the exploitation of several insights on its maximization that were here obtained. The magnetic moments are observed to couple by sizable antiferromagnetic interactions. The further step was the one where the synergic interplay of the two strategies adsorbing on Au(111) the best prototypes of 0D structures found during this study was observed. The 200 H island system was the 0D one chosen for adsorption on Au(111) and on Au(111)/G-ene. In both cases, the antiferromagnetic character was confirmed; in the latter, an almost complete retention of the magnetic moment was observed, while for the former a reduction of the 50% was computed instead. All the results presented demonstrate that G-ane islands are the most stable systems for the same number of H atoms and show a stable antiferromagnetic ground state. Our findings thus suggest that this novel and magneto-active G-ene derivative nanostructure could become achievable more easily than extended G-one or nanoribbons, with a strong potential for future spintronics applications with a variable spin-current density.

Data availability

Data of the benchmark study, including input files, output files, and metadata,[100] can be downloaded from the Novel Materials Discovery (NOMAD) Laboratory[101] under the CC-BY-4.0 license. The scripts to process the raw data and obtain the figure of merit reported in this article are publicly available.[102]

Conflicts of interest

There are no conflicts to declare.

Acknowledgements

This work was supported by the European Union through the Next Generation EU funds through the Italian MUR National

Recovery and Resilience Plan, Mission 4 Component 2 – Investment 1.4 – National Center for HPC, Big Data and Quantum Computing – CUP B83C22002830001. The support of MUR through Progetto Dipartimenti di Eccellenza 2018–2022 (CUP B96C1700020008) and 2023–2027 (CUP B97G22000740001 – DICUS 2.0). The computing resources and the related technical support used for this work have been provided by CRESCO ENEAGRID High Performance Computing infrastructure and its staff.[103] This work is partially supported by the IEMAP (Italian Energy Materials Acceleration Platform) project funded by MASE (formerly MiTE) Ministry under the international Mission Innovation initiative.[104]

Notes and references

1 R. Jansen, *J. Phys. D: Appl. Phys.*, 2003, **36**, 289–308.
2 I. Zutic, J. Fabian and S. Das Sarma, *Rev. Mod. Phys.*, 2004, **76**, 323–386.
3 M. Z. Iqbal, M. W. Iqbal, J. H. Lee, Y. S. Kim, S. H. Chun and J. Eom, *Nano Res.*, 2013, **6**, 373–380.
4 E. Coronado, *Nat. Rev. Mater.*, 2020, **5**, 87–104.
5 B. Dieny, V. S. Speriosu, S. S. Parkin, B. A. Gurney, D. R. Wilhoit and D. Mauri, *Phys. Rev. B: Condens. Matter Mater. Phys.*, 1991, **43**, 1297–1300.
6 S. Roche, J. Åkerman, B. Beschoten, J. C. Charlier, M. Chshiev, S. P. Dash, B. Dlubak, J. Fabian, A. Fert, M. Guimarães, F. Guinea, I. Grigorieva, C. Schönenberger, P. Seneor, C. Stampfer, S. O. Valenzuela, X. Waintal and B. Van Wees, *2D Materials*, 2015, **2**, 030202.
7 Z. Zanolli, *Sci. Rep.*, 2016, **6**, 1–6.
8 D. Pesin and A. H. MacDonald, *Nat. Mater.*, 2012, **11**, 409–416.
9 C. C. Lin, A. V. Penumatcha, Y. Gao, V. Q. Diep, J. Appenzeller and Z. Chen, *Nano Lett.*, 2013, **13**, 5177–5181.
10 M. Z. Iqbal, G. Hussain, S. Siddique and M. W. Iqbal, *J. Magn. Magn. Mater.*, 2017, **432**, 135–139.
11 A. Candini, S. Klyatskaya, M. Ruben, W. Wernsdorfer and M. Affronte, *Nano Lett.*, 2011, **11**, 2634–2639.
12 Y.-W. Son, M. L. Cohen and S. G. Louie, *Nature*, 2006, **444**, 347–349.
13 M. Z. Iqbal, M. W. Iqbal, X. Jin, C. Hwang and J. Eom, *J. Mater. Chem. C*, 2015, **3**, 298–302.
14 K. S. Novoselov, A. K. Geim, S. V. Morozov, D. Jiang, Y. Zhang, S. V. Dubonos, I. V. Grigorieva and A. A. Firsov, *Science*, 2004, **306**, 666–669.
15 K. S. Kim, Y. Zhao, H. Jang, S. Y. Lee, J. M. Kim, K. S. Kim, J. H. Ahn, P. Kim, J. Y. Choi and B. H. Hong, *Nature*, 2009, **457**, 706–710.
16 N. M. Peres, F. Guinea and A. H. Castro Neto, *Phys. Rev. B: Condens. Matter Mater. Phys.*, 2006, **73**, 1–23.
17 Z. Zhang, A. Kutana and B. I. Yakobson, *Nanoscale*, 2015, **7**, 2716–2722.
18 A. H. Castro Neto, F. Guinea, N. M. Peres, K. S. Novoselov and A. K. Geim, *Rev. Mod. Phys.*, 2009, **81**, 109–162.
19 K. S. Novoselov, A. K. Geim, S. V. Morozov, D. Jiang, M. I. Katsnelson, I. V. Grigorieva, S. V. Dubonos and A. A. Firsov, *Nature*, 2005, **438**, 197–200.
20 P. R. Wallace, *Phys. Rev.*, 1947, **71**, 622–634.
21 M. Y. Han, B. Özyilmaz, Y. Zhang and P. Kim, *Phys. Rev. Lett.*, 2007, **98**, 1–4.
22 T. Ohta, A. Bostwick, T. Seyller, K. Horn and E. Rotenberg, *Science*, 2006, **313**, 951–954.
23 H. Lee, K. Paeng and I. S. Kim, *Synth. Met.*, 2018, **244**, 36–47.
24 M. Pumera and Z. Sofer, *Chem. Soc. Rev.*, 2017, **46**, 4450–4463.
25 L. Liao, H. Peng and Z. Liu, *J. Am. Chem. Soc.*, 2014, **136**, 12194–12200.
26 S. Agnoli and G. Granozzi, *Surf. Sci.*, 2013, **609**, 1–5.
27 J. Hong, S. Niyogi, E. Bekyarova, M. E. Itkis, P. Ramesh, N. Amos, D. Litvinov, C. Berger, W. A. De Heer, S. Khizroev and R. C. Haddon, *Small*, 2011, **7**, 1175–1180.
28 E. J. Duplock, M. Scheffler and P. J. Lindan, *Phys. Rev. Lett.*, 2004, **92**, 1–4.
29 L. Xie, X. Wang, J. Lu, Z. Ni, Z. Luo, H. Mao, R. Wang, Y. Wang, H. Huang, D. Qi, R. Liu, T. Yu, Z. Shen, T. Wu, H. Peng, B. Özyilmaz, K. Loh, A. T. Wee, A. Ariando and W. Chen, *Appl. Phys. Lett.*, 2011, **98**, 193113.
30 W. Han, R. K. Kawakami, M. Gmitra and J. Fabian, *Nat. Nanotechnol.*, 2014, **9**, 794–807.
31 J. Wang, Y. Zhang, M. P. Sahoo, T. Shimada, T. Kitamura, P. Ghosez and T. Y. Zhang, *Sci. Rep.*, 2018, **8**, 1–9.
32 Y. Fei, S. Fang and Y. H. Hu, *Chem. Eng. J.*, 2020, **397**, 1–12.
33 D. K. Samarakoon and X. Q. Wang, *ACS Nano*, 2010, **4**, 4126–4130.
34 S. Ryu, M. Y. Han, J. Maultzsch, T. F. Heinz, P. Kim, M. L. Steigerwald and L. E. Brus, *Nano Lett.*, 2008, **8**, 4597–4602.
35 J. S. Bunch, S. S. Verbridge, J. S. Alden, A. M. Van Der Zande, J. M. Parpia, H. G. Craighead and P. L. McEuen, *Nano Lett.*, 2008, **8**, 2458–2462.
36 D. C. Elias, R. R. Nair, T. M. G. Mohiuddin, S. V. Morozov, P. Blake, M. P. Halsall, A. C. Ferrari, D. W. Boukhvalov, M. I. Katsnelson, A. K. Geim and K. S. Novoselov, *Science*, 2009, **323**, 610–613.
37 J. D. Jones, K. K. Mahajan, W. H. Williams, P. A. Ecton, Y. Mo and J. M. Perez, *Carbon*, 2010, **48**, 2335–2340.
38 A. J. Giesbers, K. Uhlírová, M. Konečný, E. C. Peters, M. Burghard, J. Aarts and C. F. Flipse, *Phys. Rev. Lett.*, 2013, **111**, 166101.
39 D. Smith, R. T. Howie, I. F. Crowe, C. L. Simionescu, C. Muryn, V. Vishnyakov, K. S. Novoselov, Y.-J. Kim, M. P. Halsall, E. Gregoryanz and J. E. Proctor, *ACS Nano*, 2015, **9**, 8279–8283.
40 M. H. Sluiter and Y. Kawazoe, *Phys. Rev. B: Condens. Matter Mater. Phys.*, 2003, **68**, 1–7.
41 J. O. Sofo, A. S. Chaudhari and G. D. Barber, *Phys. Rev. B: Condens. Matter Mater. Phys.*, 2007, **75**, 1–4.
42 F. Buonocore, A. Capasso and N. Lisi, *Mater. Res. Express*, 2014, **1**, 15608.
43 O. Leenaerts, H. Peelaers, A. D. Hernández-Nieves, B. Partoens and F. M. Peeters, *Phys. Rev. B: Condens. Matter Mater. Phys.*, 2010, **82**, 1–6.
44 M. Pumera and C. H. An Wong, *Chem. Soc. Rev.*, 2013, **42**, 5987–5995.

45 L. Feng and W. X. Zhang, *AIP Adv.*, 2012, **2**, 1–6.
46 R. Balog, B. Jørgensen, L. Nilsson, M. Andersen, E. Rienks, M. Bianchi, M. Fanetti, E. Lægsgaard, A. Baraldi, S. Lizzit, Z. Sljivancanin, F. Besenbacher, B. Hammer, T. G. Pedersen, P. Hofmann and L. Hornekær, *Nat. Mater.*, 2010, **9**, 315–319.
47 Y. Song, K. Qian, L. Tao, Z. Wang, H. Guo, H. Chen, S. Zhang, Y.-Y. Zhang, X. Lin, S. T. Pantelides, S. Du and H.-J. Gao, *Small*, 2022, **18**, 2102687.
48 W. K. Lee, K. E. Whitener, J. T. Robinson and P. E. Sheehan, *Adv. Mater.*, 2015, **27**, 1774–1778.
49 J. Son, S. Lee, S. J. Kim, B. C. Park, H. K. Lee, S. Kim, J. H. Kim, B. H. Hong and J. Hong, *Nat. Commun.*, 2016, **7**, 1–7.
50 J. Berashevich and T. Chakraborty, *Nanotechnology*, 2010, **21**, 1–5.
51 R. R. Nair, M. Sepioni, I. L. Tsai, O. Lehtinen, J. Keinonen, A. V. Krasheninnikov, T. Thomson, A. K. Geim and I. V. Grigorieva, *Nat. Phys.*, 2012, **8**, 199–202.
52 J. Tuček, K. Holá, A. B. Bourlinos, P. Błoński, A. Bakandritsos, J. Ugolotti, M. Dubecký, F. Karlický, V. Ranc, K. Čépe, M. Otyepka and R. Zbořil, *Nat. Commun.*, 2017, **8**, 1–12.
53 A. Ney, P. Papakonstantinou, A. Kumar, N. G. Shang and N. Peng, *Appl. Phys. Lett.*, 2011, **99**, 2–5.
54 J. Zhou, Q. Wang, Q. Sun, X. S. Chen, Y. Kawazoe and P. Jena, *Nano Lett.*, 2009, **9**, 3867–3870.
55 M. Wojtaszek, N. Tombros, A. Caretta, P. H. Van Loosdrecht and B. J. Van Wees, *J. Appl. Phys.*, 2011, **110**, 1–7.
56 K. E. Whitener, *J. Vac. Sci. Technol., A*, 2018, **36**, 05G401.
57 B. Li, L. Zhou, D. Wu, H. Peng, K. Yan, Y. Zhou and Z. Liu, *ACS Nano*, 2011, **5**, 5957–5961.
58 N. Watanabe, T. Nakajima and N. Ohsawa, *Bull. Chem. Soc. Jpn.*, 1982, **55**, 2029–2033.
59 D. K. Samarakoon and X.-Q. Wang, *ACS Nano*, 2009, **3**, 4017–4022.
60 C. Zhou, S. Chen, J. Lou, J. Wang, Q. Yang, C. Liu, D. Huang and T. Zhu, *Nanoscale Res. Lett.*, 2014, **9**, 1–9.
61 R. Hoffmann, *Rev. Mod. Phys.*, 1988, **60**, 601–628.
62 A. Caneschi, D. Gatteschi and F. Totti, *Coord. Chem. Rev.*, 2015, **289–290**, 357–378.
63 J. Hutter, M. Iannuzzi, F. Schiffmann and J. Vandevondele, *Wiley Interdiscip. Rev.: Comput. Mol. Sci.*, 2014, **4**, 15–25.
64 J. VandeVondele, M. Krack, F. Mohamed, M. Parrinello, T. Chassaing and J. Hutter, *Comput. Phys. Commun.*, 2005, **167**, 103–128.
65 T. D. Kühne, M. Iannuzzi, M. Del Ben, V. V. Rybkin, P. Seewald, F. Stein, T. Laino, R. Z. Khaliullin, O. Schütt, F. Schiffmann, D. Golze, J. Wilhelm, S. Chulkov, M. H. Bani-Hashemian, V. Weber, U. Borštnik, M. Taillefumier, A. S. Jakobovits, A. Lazzaro, H. Pabst, T. Müller, R. Schade, M. Guidon, S. Andermatt, N. Holmberg, G. K. Schenter, A. Hehn, A. Bussy, F. Belleflamme, G. Tabacchi, A. Glöß, M. Lass, I. Bethune, C. J. Mundy, C. Plessl, M. Watkins, J. VandeVondele, M. Krack and J. Hutter, *J. Chem. Phys.*, 2020, **152**, 194103.
66 S. Goedecker, M. Teter and J. Hutter, *Phys. Rev. B: Condens. Matter Mater. Phys.*, 1996, **54**, 1703–1710.
67 C. Hartwigsen, S. Goedecker and J. Hutter, *Phys. Rev. B: Condens. Matter Mater. Phys.*, 1998, **58**, 3641–3662.
68 M. Krack, *Theor. Chem. Acc.*, 2005, **114**, 145–152.
69 J. P. Perdew, K. Burke and M. Ernzerhof, *Phys. Rev. Lett.*, 1996, **77**, 3865.
70 Y. Zhang and W. Yang, *Phys. Rev. Lett.*, 1998, **80**, 890.
71 R. Sabatini, T. Gorni and S. De Gironcoli, *Phys. Rev. B: Condens. Matter Mater. Phys.*, 2013, **87**, 041108.
72 M. P. Teter, M. C. Payne and D. C. Allan, *Phys. Rev. B: Condens. Matter Mater. Phys.*, 1989, **40**, 12255–12263.
73 G. Santarossa, A. Vargas, M. Iannuzzi, C. A. Pignedoli, D. Passerone and A. Baiker, *J. Chem. Phys.*, 2008, **129**, 234703.
74 I. Cimatti, L. Bondì, G. Serrano, L. Malavolti, B. Cortigiani, E. Velez-Fort, D. Betto, A. Ouerghi, N. B. Brookes, S. Loth, M. Mannini, F. Totti and R. Sessoli, *Nanoscale Horiz.*, 2019, **4**, 1202–1210.
75 G. Serrano, L. Poggini, M. Briganti, A. L. Sorrentino, G. Cucinotta, L. Malavolti, B. Cortigiani, E. Otero, P. Sainctavit, S. Loth, F. Parenti, A.-L. Barra, A. Vindigni, A. Cornia, F. Totti, M. Mannini and R. Sessoli, *Nat. Mater.*, 2020, **19**, 546–551.
76 L. Bondì, S. Brooker and F. Totti, *J. Mater. Chem. C*, 2021, **9**, 14256–14268.
77 G. Lippert, J. Hutter and M. Parrinello, *Mol. Phys.*, 1997, **92**, 477–487.
78 G. Lippert, J. J. Hutter and M. Parrinello, *Theor. Chem. Acc.*, 1999, **103**, 124–140.
79 P. Kratzer and J. Neugebauer, *Front. Chem.*, 2019, **7**, 1–18.
80 S. Casolo, O. M. Løvvik, R. Martinazzo and G. F. Tantardini, *J. Chem. Phys.*, 2009, **130**, 1–10.
81 F. Neese, *Coord. Chem. Rev.*, 2009, **253**, 526–563.
82 L. Noodleman, C. Y. Peng, D. A. Case and J. M. Mouesca, *Coord. Chem. Rev.*, 1995, **144**, 199–244.
83 A. Bencini, F. Totti, C. A. Daul, K. Doclo, P. Fantucci and V. Barone, *Inorg. Chem.*, 1997, **36**, 5022–5030.
84 A. Bencini and F. Totti, *J. Chem. Theory Comput.*, 2009, **5**, 144–154.
85 M. Birowska, M. E. Marchwiany, C. Draxl and J. A. Majewski, *Comput. Mater. Sci.*, 2021, **186**, 109940.
86 F. Buonocore, A. Mosca Conte and N. Lisi, *Phys. E*, 2016, **78**, 65–72.
87 M. Birowska, K. Milowska and J. A. Majewski, *Acta Phys. Pol., A*, 2011, **120**, 845–848.
88 H. Şahin, C. Ataca and S. Ciraci, *Appl. Phys. Lett.*, 2009, **95**, 1–3.
89 A. I. Podlivaev and L. A. Openov, *Semiconductors*, 2011, **45**, 958–961.
90 L. A. Openov and A. I. Podlivaev, *JETP Lett.*, 2009, **90**, 459–463.
91 M. J. Schmidt and D. Loss, *Phys. Rev. B: Condens. Matter Mater. Phys.*, 2010, **82**, 1–13.
92 V. Tozzini and V. Pellegrini, *Phys. Rev. B: Condens. Matter Mater. Phys.*, 2010, **81**, 22–25.

93 M. Z. Flores, P. A. Autreto, S. B. Legoas and D. S. Galvao, *Nanotechnology*, 2009, **20**, 1–6.
94 A. G. Villalba, PhD thesis, Université Bourgogne Franche-Comté, 2017.
95 A. D. Hernández-Nieves, B. Partoens and F. M. Peeters, *Phys. Rev. B: Condens. Matter Mater. Phys.*, 2010, **82**, 1–9.
96 J. H. Lee and J. C. Grossman, *Appl. Phys. Lett.*, 2010, **97**, 19–22.
97 S. Okada, *Phys. Rev. B: Condens. Matter Mater. Phys.*, 2008, **77**, 1–4.
98 P. Koskinen, S. Malola and H. Häkkinen, *Phys. Rev. B: Condens. Matter Mater. Phys.*, 2009, **80**, 16–18.
99 V. Georgakilas, J. A. Perman, J. Tucek and R. Zboril, *Chem. Rev.*, 2015, **115**, 4744–4822.
100 A. Albino, F. Buonocore, M. Celino, F. Totti, *Dataset in NOMAD repository*, 2024, DOI: **10.17172/NOMAD/2024.01.09-2**.
101 M. Scheidgen, L. Himanen, A. N. Ladines, D. Sikter, M. Nakhaee, Á. Fekete, T. Chang, A. Golparvar, J. A. Márquez, S. Brockhauser, S. Brückner, L. M. Ghiringhelli, F. Dietrich, D. Lehmberg, T. Denell, A. Albino, H. Näsström, S. Shabih, F. Dobener, M. Kühbach, R. Mozumder, J. F. Rudzinski, N. Daelman, J. M. Pizarro, M. Kuban, C. Salazar, P. Ondračka, H.-J. Bungartz and C. Draxl, *J. Open Source Softw.*, 2023, **8**, 5388.
102 **https://github.com/aalbino2/CP2K_graphone_analysis**.
103 F. Iannone, F. Ambrosino, G. Bracco, M. D. Rosa, A. Funel, G. Guarnieri, S. Migliori, F. Palombi, G. Ponti, G. Santomauro and P. Procacci, *2019 International Conference on High Performance Computing and Simulation*, 2019, pp. 1051–1052.
104 A. Aspuru-Guzik and K. Persson, *Mission Innovation*, 2018.